



An unconditionally stable semi-implicit FSI finite element method[☆]

Alexander Lozovskiy^a, Maxim A. Olshanskii^{b,*}, Victoria Salamatova^c,
Yuri V. Vassilevski^c

^a Department of Mathematics, Texas A&M University, United States

^b Department of Mathematics, University of Houston, United States

^c Moscow Institute of Physics and Technology and Institute of Numerical Mathematics RAS, Russia

Received 16 May 2015; received in revised form 14 September 2015; accepted 19 September 2015

Available online 28 September 2015

Highlights

- We devise an unconditionally stable FSI numerical method based on ALE monolithic formulation.
- On every time step the method is linear.
- Incompressible and slightly compressible neo-Hookean models are numerically compared for a model hemodynamic problem.

Abstract

The paper addresses the numerical solution of fluid–structure interaction (FSI) problems involving incompressible viscous Newtonian fluid and hyperelastic material. A well known challenge in computing FSI systems is to provide an effective time-marching algorithm, which avoids numerical instabilities due to the loose coupling of fluid and structure motion on the FSI interface. In this work, we introduce a semi-implicit finite element scheme for an Arbitrary Lagrangian–Eulerian formulation of the fluid–structure interaction problem. The approach strongly enforces the coupling conditions on the fluid–structure interface, but requires only a linear problem to be solved on each time step. Further, we prove that the numerical solution to the fully discrete problem satisfies the correct energy balance, and the stability estimate follows without any extra model simplifications or assumptions on the time step. The analysis covers the cases of Saint Venant–Kirchhoff compressible and incompressible neo-Hookean materials. Results of several numerical experiments are included to illustrate the properties of the method and its applicability for the simulation of certain hemodynamic flows. We also experiment with the enforcement of material incompressibility condition in the finite element method via an integral constraint or alternatively letting the Poisson ratio in the compressible model to be close to $\frac{1}{2}$. From these experiments conclusions are drawn concerning the accuracy of flow statistics prediction for incompressible vs. nearly incompressible structure models.

© 2015 Elsevier B.V. All rights reserved.

Keywords: Fluid–structure interaction; Semi-implicit scheme; Monolithic approach; Blood flow; Numerical stability; Finite element method

[☆] This work has been supported by the Russian Science Foundation (RSF) grant 14-31-00024.

* Corresponding author.

E-mail addresses: lozovskiy@math.tamu.edu (A. Lozovskiy), molshan@math.uh.edu (M.A. Olshanskii), salamatova@gmail.com (V. Salamatova), yuri.vassilevski@gmail.com (Y.V. Vassilevski).

1. Introduction

Fluid–structure interaction phenomena is of great importance in many engineering and life science applications. Among these applications, hemodynamic and cardiovascular FSI problems received recently much attention, see, e.g., [1–3]. In this paper, we address the numerical solution of a fluid–structure interaction problem involving a viscous incompressible fluid and hyperelastic compressible and incompressible materials. This model is often used to describe blood motion in compliant vessels and the heart.

Two major approaches to the solution of FSI problem can be distinguished: the monolithic approach and the partitioned one. In the scope of the monolithic approach [4–8], the fluid and the structure are treated as a single continuum, and the coupling conditions at interface are implicit for the solution procedure. The partitioned approach [4,9–12] treats the fluid and the structure separately. In the course of simulation, one consequently solves fluid and structure subproblems, using the computed forces of the one subproblem as boundary conditions for the other subproblem. One known issue of the partitioned approach is that the accuracy of satisfying the coupling conditions at the interface between the fluid and the structure may effect significantly the numerical stability of the method. At the same time, monolithic approaches are generally more demanding for efficient algebraic solvers and require more implementation effort if a legacy CFD code is used.

Following a common convention, we call a numerical FSI algorithm strongly coupled, if the interface conditions are exactly satisfied at every time step. Otherwise, we call it a loosely or weakly coupled algorithm. It is well-known that a weak coupling may lead to numerical instabilities due to added-mass effect [13,14]. Strongly coupled methods are generally more stable, but computationally more demanding. Note that it is possible to enforce the strong coupling for partitioned solvers, but it can be expensive due to slow convergence of iterations between subdomains [15]; see also [16] for optimization based enforcement of coupling conditions in partitioned solvers. This paper studies a strongly coupled algorithm within a monolithic finite element approach. The reduction of computational costs is achieved by an extrapolation technique leading to a semi-implicit method, which requires only one linear problem to be solved on every time step. Numerical analysis of a finite element method for the FSI problem is challenging due to the non-linearity of the system and its mixed hyperbolic–parabolic type. Several results on stability of finite element solutions are known in the literature, and for most of them the time-stepping scheme has to be implicit in fluid–structure coupling and geometry advancing. Thus, in [17] energy stability of a second order implicit finite element method was proved. In the same reference, a stability estimate subject to a time-step restriction was proved for a semi-implicit algorithm based on the Leap-Frog discretization for the structure and on the implicit Euler discretization for the fluid. In order to linearize the convection term of the Navier–Stokes equation, a supplementary fluid problem has to be solved. In [18], an algorithm based on the Chorin–Temam projection scheme for incompressible flows is proposed. On each time-step, the algorithm is linear in convection–diffusion and nonlinear in projection sub-steps because of the implicit coupling to the structure equation. The stability was proved when the fluid domain is fixed. In the present paper, we show correct energy balance and prove the unconditional (without a time-step restriction) stability of a finite-element FSI method, which treats geometric non-linearities in an explicit way and linearizes fluid inertia terms. The analysis is applied to the fully discrete formulation of a 3D FSI problem with hyperelastic compressible and incompressible models for the material. We note that stability of FSI finite element schemes with time-lagged geometric non-linearities was previously observed in numerical experiments, see, e.g., [19], but the analysis was available only for simplified FSI problems [20,21].

Numerical FSI approaches may employ either conforming meshes fitted to fluid–structure interface or non-conforming (unfitted) meshes [4]. In the present study, we use a mesh fitted to the structure. The Arbitrary Lagrangian–Eulerian (ALE) formulation [22–24] of the FSI problem is employed. Both fluid and structure equations are discretized in a reference domain and so mesh reconstruction is avoided. This limits the present approach to the case of modest (but not necessarily ‘small’) deformations and does not allow topological changes.

The paper also aims at the application of the developed numerical methodology in hemodynamic simulations such as the computing of incompressible viscous fluid flow in a deformable vessel. This application of FSI numerical techniques received significant attention in the literature, see, e.g., [17,25–27]. In numerical simulations, vessel walls are often modeled using a thin shell approximation, while in reality, the blood vessel wall thickness can be significant, cf., e.g., [28], and accounting for this is important for obtaining physiologically relevant solutions to hemodynamic problems. Here we treat the vessel wall as a hyperelastic body. Accurate simulation of mechanical properties of blood vessel walls such as nonlinear constitutive equation and near incompressibility [29] challenges an FSI numerical

method. While the question of vessel wall compressibility is not ultimately answered by now, it is often accepted that the wall is an incompressible material. At the same time, recent experimental research shows that relative compressibility of vessel wall may be as large as 2%–6% under physiological pressure range [30]. Results in [31] show that the effect of arterial compressibility (about 3%) may lead to notable difference in observed displacement and stress values. Thus, we experiment numerically with both incompressible and slightly compressible elasticity models. The results presented in Section 5 show, in particular, that for a Poisson ratio close to $\frac{1}{2}$ a compressible neo-Hookean model reproduces the statistics of the incompressible model rather accurately for the monolithic finite element approach. If the incompressibility constraint for the structure and for the fluid is enforced weakly in the finite element method, then the corresponding Lagrange multiplier (having a physical meaning of pressure in fluid domain) should admit discontinuity across the fluid–structure interface. Globally continuous Lagrange multiplier finite element space may affect significantly the accuracy of the numerical simulation.

Summarizing, the present paper studies a monolithic strongly coupled finite element method for the ALE formulation of FSI problem. The proposed scheme is second order accurate in time and requires solving only a linear system of algebraic equations per time step. For the first order in time counterpart of the method, we prove the energy stability without restrictions on time step. Results of the numerical experiments suggest that the second order variant of the method is also stable. The energy estimate is shown if the fluid is incompressible Newtonian and the structure is described by Saint Venant–Kirchhoff or incompressible neo-Hookean constitutive laws. FSI models with incompressible and slightly compressible neo-Hookean materials are compared in numerical experiments.

The outline of the remainder of the paper is the following. In Section 2 we recall the governing equations for the monolithic ALE formulation and introduce necessary preliminaries. In Section 3 we introduce the finite element method and the semi-implicit scheme. The method is analyzed in Section 4, where suitable a priori energy estimates for numerical solutions are shown. Results of numerical experiments for two-dimensional FSI problems are presented and discussed in Section 5. The method is implemented using the open source package Ani2D [32]. Section 6 collects a few closing remarks.

2. FSI model

Consider a time-dependent domain $\Omega(t) \subset \mathbb{R}^N$, $N = 2, 3$, partitioned into a subdomain $\Omega^f(t)$ occupied by fluid and $\Omega^s(t)$ occupied by solid. Let $\Gamma^{fs}(t) := \partial\Omega^f(t) \cap \partial\Omega^s(t)$ be the interface where the interaction of the fluid and solid takes place. Denote the reference domains by

$$\Omega_f = \Omega^f(0), \quad \Omega_s = \Omega^s(0), \quad \Gamma_{fs} = \Gamma^{fs}(0),$$

and the deformation of the solid medium by

$$\xi^s : \Omega_s \times [0, t] \rightarrow \bigcup_{t \in [0, T]} \Omega^s(t),$$

with the corresponding displacement \mathbf{u}^s given by $\mathbf{u}^s(\mathbf{x}, t) := \mathbf{x} - \xi^s(\mathbf{x}, t)$ and velocity $\mathbf{v}^s = \partial_t \mathbf{u}^s = -\partial_t \xi^s(\mathbf{x}, t)$.

The fluid dynamics is described by the velocity vector field $\mathbf{v}^f(\mathbf{x}, t)$ and the pressure function $p^f(\mathbf{x}, t)$ defined in $\Omega^f(t)$ for $t \in [0, T]$. In this paper, we adopt the Arbitrary Lagrangian–Eulerian formulation by introducing another auxiliary mapping

$$\xi^f : \Omega_f \times [0, t] \rightarrow \bigcup_{t \in [0, T]} \Omega^f(t)$$

such that $\xi^s = \xi^f$ on Γ_{fs} . In general, ξ^f does not follow material trajectories. Instead, it is defined by a continuous extension of the displacement field to the flow reference domain

$$\mathbf{u}^f := \text{Ext}(\mathbf{u}^s) = \mathbf{x} - \xi^f(\mathbf{x}, t) \quad \text{in } \Omega_f \times [0, t]. \tag{1}$$

Furthermore, assume no-slip no-penetration boundary conditions on the fluid–structure interface:

$$\mathbf{v}^s = \mathbf{v}^f \quad \text{on } \Gamma_{fs}. \tag{2}$$

Following [5] we consider a monolithic numerical approach using the continuous globally defined displacement and velocity fields

$$\mathbf{u} = \begin{cases} \mathbf{u}^s & \text{in } \Omega_s, \\ \mathbf{u}^f & \text{in } \Omega_f, \end{cases} \quad \mathbf{v} = \begin{cases} \mathbf{v}^s & \text{in } \Omega_s, \\ \mathbf{v}^f & \text{in } \Omega_f. \end{cases}$$

The corresponding globally defined deformation gradient is $\mathbf{F} = \mathbf{I} + \nabla \mathbf{u}$. Its determinant will be denoted by $J := \det(\mathbf{F})$.

Denote by ρ_s and $\rho_f = \text{const}$ the densities of solid and fluid, and by $\boldsymbol{\sigma}_s, \boldsymbol{\sigma}_f$ the Cauchy stress tensors, so that $J(\boldsymbol{\sigma}_s \circ \boldsymbol{\xi}^s) \mathbf{F}^{-T}$ is the Piola–Kirchhoff tensor in the structure, $\boldsymbol{\sigma}_s \circ \boldsymbol{\xi}^s(\mathbf{x}) := \boldsymbol{\sigma}_s(\boldsymbol{\xi}^s(\mathbf{x}))$.

The dynamic equations for the fluid and structure in the reference domains read

$$\frac{\partial \mathbf{v}}{\partial t} = \begin{cases} \rho_s^{-1} \text{div}(J(\boldsymbol{\sigma}_s \circ \boldsymbol{\xi}^s) \mathbf{F}^{-T}) & \text{in } \Omega_s, \\ (J\rho_f)^{-1} \text{div}(J(\boldsymbol{\sigma}_f \circ \boldsymbol{\xi}^f) \mathbf{F}^{-T}) - (\nabla \mathbf{v}) \left(\mathbf{F}^{-1} \left(\mathbf{v} - \frac{\partial \mathbf{u}}{\partial t} \right) \right) & \text{in } \Omega_f. \end{cases} \quad (3)$$

The definition of \mathbf{v} in the solid domain gives

$$\frac{\partial \mathbf{u}}{\partial t} = \mathbf{v} \quad \text{in } \Omega_s. \quad (4)$$

The fluid is assumed incompressible. The mass conservation of fluid leads to the equation in the reference domain:

$$\text{div}(J\mathbf{F}^{-1}\mathbf{v}) = 0 \quad \text{in } \Omega_f. \quad (5)$$

In addition to (2), the balance of normal stresses provides the second interface condition:

$$\boldsymbol{\sigma}_f \mathbf{F}^{-T} \mathbf{n} = \boldsymbol{\sigma}_s \mathbf{F}^{-T} \mathbf{n} \quad \text{on } \Gamma_{fs}. \quad (6)$$

The boundary of $\Omega(0)$ is subdivided into the structure boundary $\Gamma_{s0} := \partial\Omega(0) \cap \partial\Omega_s$, fluid Dirichlet and outflow boundaries: $\partial\Omega(0) \cap \partial\Omega_f = \Gamma_{f0} \cup \Gamma_{\text{out}}$. The governing equations are complemented with boundary conditions

$$\mathbf{v} = \mathbf{g} \quad \text{on } \Gamma_{f0}, \quad \boldsymbol{\sigma}_f \mathbf{F}^{-T} \mathbf{n} = \mathbf{0} \quad \text{on } \Gamma_{\text{out}}, \quad \mathbf{u} = \mathbf{0} \quad \text{on } \Gamma_{s0} \cup \Gamma_{f0} \cup \Gamma_{\text{out}}, \quad (7)$$

and initial conditions

$$\mathbf{u}(\mathbf{x}, 0) = \mathbf{0} \quad \text{on } \Omega(0), \quad \mathbf{v}(\mathbf{x}, 0) = \mathbf{v}_0(\mathbf{x}) \quad \text{in } \Omega(0). \quad (8)$$

We assume the fluid to be Newtonian, with the viscosity parameter μ_f . In the reference domain the constitutive relation for the fluid reads

$$\boldsymbol{\sigma}_f = -p_f \mathbf{I} + \mu_f (\nabla \mathbf{v} \mathbf{F}^{-1} + \mathbf{F}^{-T} (\nabla \mathbf{v})^T) \quad \text{in } \Omega_f. \quad (9)$$

For the structure we consider two hyperelastic materials. The first one is the compressible geometrically nonlinear Saint Venant–Kirchhoff material with

$$\boldsymbol{\sigma}_s = \frac{1}{J} \mathbf{F} (\lambda_s \text{tr}(\mathbf{E}) \mathbf{I} + 2\mu_s \mathbf{E}) \mathbf{F}^T, \quad (10)$$

where $\mathbf{E} = \frac{1}{2} (\mathbf{F}^T \mathbf{F} - \mathbf{I})$ is the Lagrange–Green strain tensor and λ_s, μ_s are the Lamé constants. The second one is the incompressible neo-Hookean material with

$$\boldsymbol{\sigma}_s = \mu_s \mathbf{F} \mathbf{F}^T - p_s \mathbf{I}, \quad (11)$$

and a new multiplier p_s . The first Piola–Kirchhoff tensor for the incompressible material can be written as

$$J \boldsymbol{\sigma}_s \mathbf{F}^{-T} = \mu_s \mathbf{F} - J p_s \mathbf{F}^{-T}.$$

For the notation convenience, we set $p_s = 0$ in Ω_s for the compressible structure and define the global pressure variable by

$$p = \begin{cases} p_f & \text{in } \Omega_f, \\ p_s & \text{in } \Omega_s. \end{cases}$$

Thus, the FSI problem in the reference coordinates consists in finding pressure distribution p and continuous velocity and displacement fields \mathbf{v} , \mathbf{u} satisfying the set of equations, interface and boundary conditions (3)–(9), together with (10) or (11), and subject to a given extension rule (1).

Before recalling the energy balance of the FSI problem, we note a few identities that are useful for the design of a numerical method and its analysis. The mass balance yields in the fluid region the equality

$$\frac{\partial J}{\partial t} + \operatorname{div} \left(J \mathbf{F}^{-1} \left(\mathbf{v} - \frac{\partial \mathbf{u}}{\partial t} \right) \right) = 0 \quad \text{in } \Omega_f. \tag{12}$$

The Piola identity $\operatorname{div} (J \mathbf{F}^{-1}) = 0$ implies the following equality

$$\operatorname{div} (J \mathbf{F}^{-1} \mathbf{v}) = J (\nabla \mathbf{v}) : \mathbf{F}^{-T} \quad \text{in } \Omega_f, \tag{13}$$

where $\mathbf{A} : \mathbf{B} := \sum_{i,j=1}^N A_{ij} B_{ij}$. For the incompressible homogeneous material, i.e. $J = 1$ and $\rho_s = \text{const}$, the Piola identity also yields

$$J (\nabla \mathbf{v}) : \mathbf{F}^{-T} = 0 \quad \text{in } \Omega_s. \tag{14}$$

2.1. Energy equality

For the brevity, assume the homogeneous boundary conditions, i.e. $\mathbf{g} = 0$. We make use of the identity:

$$\int_{\Omega_f} ((\mathbf{w} \cdot \nabla u))v + \frac{1}{2} ((\operatorname{div} \mathbf{w})uv) \, d\mathbf{x} = \int_{\Omega_f} \frac{1}{2} ((\mathbf{w} \cdot \nabla u)v - (\mathbf{w} \cdot \nabla v)u) \, d\mathbf{x} + \frac{1}{2} \int_{\partial \Omega_f} (\mathbf{n} \cdot \mathbf{w})uv \, ds. \tag{15}$$

Multiplying the first equality in (3) by $\rho_s \mathbf{v}$, the second one by $J \rho_f \mathbf{v}$, integrating over the reference domain, and employing (15) gives

$$\begin{aligned} & \frac{1}{2} \frac{d}{dt} \left(\int_{\Omega_s} \rho_s |\mathbf{v}|^2 \, d\mathbf{x} + \rho_f \int_{\Omega_f} J |\mathbf{v}|^2 \, d\mathbf{x} \right) - \frac{\rho_f}{2} \int_{\Omega_f} \frac{\partial J}{\partial t} |\mathbf{v}|^2 \, d\mathbf{x} \\ & + \int_{\Omega_s} J (\boldsymbol{\sigma}_s \circ \boldsymbol{\xi}^s) \mathbf{F}^{-T} : \nabla \mathbf{v} \, d\mathbf{x} + \int_{\Omega_f} J (\boldsymbol{\sigma}_f \circ \boldsymbol{\xi}^f) \mathbf{F}^{-T} : \nabla \mathbf{v} \, d\mathbf{x} \\ & - \frac{\rho_f}{2} \int_{\Omega_f} \operatorname{div} \left(J \mathbf{F}^{-1} \left(\mathbf{v} - \frac{\partial \mathbf{u}}{\partial t} \right) \right) |\mathbf{v}|^2 \, d\mathbf{x} + \frac{\rho_f}{2} \int_{\Gamma_{\text{out}}} \mathbf{v} \cdot \mathbf{n} |\mathbf{v}|^2 \, ds = 0. \end{aligned}$$

The identity (12) leads to some cancellations and we get

$$\begin{aligned} & \frac{1}{2} \frac{d}{dt} \left(\int_{\Omega_s} \rho_s |\mathbf{v}|^2 \, d\mathbf{x} + \rho_f \int_{\Omega_f} J |\mathbf{v}|^2 \, d\mathbf{x} \right) + \int_{\Omega_s} J (\boldsymbol{\sigma}_s \circ \boldsymbol{\xi}^s) \mathbf{F}^{-T} : \nabla \mathbf{v} \, d\mathbf{x} \\ & + \int_{\Omega_f} J (\boldsymbol{\sigma}_f \circ \boldsymbol{\xi}^f) \mathbf{F}^{-T} : \nabla \mathbf{v} \, d\mathbf{x} + \frac{\rho_f}{2} \int_{\Gamma_{\text{out}}} \mathbf{v} \cdot \mathbf{n} |\mathbf{v}|^2 \, ds = 0. \end{aligned}$$

For the Saint Venant–Kirchhoff problem, we can rewrite the third term as

$$\begin{aligned} \int_{\Omega_s} J (\boldsymbol{\sigma}_s \circ \boldsymbol{\xi}^s) \mathbf{F}^{-T} : \nabla \mathbf{v} \, d\mathbf{x} &= \int_{\Omega_s} J (\boldsymbol{\sigma}_s \circ \boldsymbol{\xi}^s) \mathbf{F}^{-T} : \nabla \frac{\partial \mathbf{u}}{\partial t} \, d\mathbf{x} \\ &= \int_{\Omega_s} J (\boldsymbol{\sigma}_s \circ \boldsymbol{\xi}^s) \mathbf{F}^{-T} : \frac{\partial \mathbf{F}}{\partial t} \, d\mathbf{x} = \int_{\Omega_s} \mathbf{F} (\lambda_s \operatorname{tr}(\mathbf{E}) + 2\mu_s \mathbf{E}) : \frac{\partial \mathbf{F}}{\partial t} \, d\mathbf{x} \end{aligned}$$

$$\begin{aligned}
&= \int_{\Omega_s} (\lambda_s \text{tr}(\mathbf{E})\mathbf{I} + 2\mu_s \mathbf{E}) : \mathbf{F}^T \frac{\partial \mathbf{F}}{\partial t} \, d\mathbf{x} = \frac{1}{2} \int_{\Omega_s} (\lambda_s \text{tr}(\mathbf{E})\mathbf{I} + 2\mu_s \mathbf{E}) : \frac{\partial (\mathbf{F}^T \mathbf{F})}{\partial t} \, d\mathbf{x} \\
&= \int_{\Omega_s} (\lambda_s \text{tr}(\mathbf{E})\mathbf{I} + 2\mu_s \mathbf{E}) : \frac{\partial \mathbf{E}}{\partial t} \, d\mathbf{x} = \frac{1}{2} \frac{d}{dt} \int_{\Omega_s} (\lambda_s \text{tr}(\mathbf{E})^2 + 2\mu_s |\mathbf{E}|_F^2) \, d\mathbf{x}.
\end{aligned}$$

Here and in the remainder, $|\dots|_F$ stands for the Frobenius norm. Using the notation $\widehat{\mathbf{D}}(\mathbf{v}) = \frac{1}{2}(\nabla \mathbf{v} \mathbf{F}^{-1} + \mathbf{F}^{-T}(\nabla \mathbf{v})^T)$ for the rate of deformation tensor in the ALE coordinates, we get with the help of (5) and (13)

$$\int_{\Omega_f} J(\boldsymbol{\sigma}_f \circ \boldsymbol{\xi}^f) \mathbf{F}^{-T} : \nabla \mathbf{v} \, d\mathbf{x} = 2\mu_f \int_{\Omega_f} J |\widehat{\mathbf{D}}(\mathbf{v})|_F^2 \, d\mathbf{x}.$$

Therefore, the energy equality in ALE coordinates takes the form

$$\begin{aligned}
&\frac{1}{2} \frac{d}{dt} \left(\int_{\Omega_s} \rho_s \left| \frac{\partial \mathbf{u}}{\partial t} \right|^2 \, d\mathbf{x} + \rho_f \int_{\Omega_f} J |\mathbf{v}|^2 \, d\mathbf{x} + \int_{\Omega_s} (\lambda_s \text{tr}(\mathbf{E})^2 + 2\mu_s |\mathbf{E}|_F^2) \, d\mathbf{x} \right) \\
&+ 2\mu_f \int_{\Omega_f} J |\widehat{\mathbf{D}}(\mathbf{v})|_F^2 \, d\mathbf{x} + \frac{\rho_f}{2} \int_{\Gamma_{\text{out}}} \mathbf{v} \cdot \mathbf{n} |\mathbf{v}|^2 \, ds = 0, \tag{16}
\end{aligned}$$

i.e. the variation of the total system energy is balanced by the fluid viscous dissipation and the energy rate at the open boundary. For the FSI problem with the incompressible neo-Hookean material, the energy balance takes the same form with the potential energy of the structure (third term in (16)) equal $\int_{\Omega_s} \mu_s |\mathbf{F}|_F^2 \, d\mathbf{x}$. We shall look whether the energy balance of our numerical method resembles (16).

3. Discretization method

In this section we introduce both time and space discretization of the FSI problem. Treating the problem in reference coordinates allows us to avoid triangulations and finite element function spaces dependent on time. For an alternative approach based on space–time finite element methods see, for example, [33,34]. Thus, consider a collection of simplexes (triangles in 2D and tetrahedra in 3D), which form a consistent regular triangulation of the reference domain $\overline{\Omega}(0) = \overline{\Omega}_s \cup \overline{\Omega}_f$. In the monolithic approach we consider conforming FE spaces $\mathbb{V}_h \subset H^1(\Omega(0))^N$ and $\mathbb{Q}_h \subset L^2(\Omega(0))$ for trial functions and the following two subspaces for the test functions: $\mathbb{V}_h^0 = \{\mathbf{v} \in \mathbb{V}_h : \mathbf{v}|_{\Gamma_{s0} \cup \Gamma_{f0}} = \mathbf{0}\}$ and $\mathbb{V}_h^{00} = \{\mathbf{v} \in \mathbb{V}_h^0 : \mathbf{v}|_{\Gamma_{sf}} = \mathbf{0}\}$. We assume that \mathbb{V}_h^0 and \mathbb{Q}_h form the LBB-stable finite element pair: There exists a mesh-independent constant c_0 , such that

$$\inf_{q_h \in \mathbb{Q}_h} \sup_{\mathbf{v}_h \in \mathbb{V}_h^0} \frac{(q_h, \text{div } \mathbf{v}_h)}{\|\nabla \mathbf{v}_h\| \|q_h\|} \geq c_0 > 0.$$

Assuming a constant time step Δt , we use the notation $\mathbf{u}^k(\mathbf{x}) \approx \mathbf{u}(k\Delta t, \mathbf{x})$, and similar for \mathbf{v} and p .

To formulate the discretization method, we need some further notations. For a tensor $\mathbf{A} \in \mathbb{R}^{N \times N}$, we denote its symmetric part as $\{\mathbf{A}\}_s = \frac{1}{2}(\mathbf{A} + \mathbf{A}^T)$. We shall emphasize the dependence on a displacement field in $\mathbf{F}(\mathbf{u}) := \mathbf{I} + \nabla \mathbf{u}$ and set

$$\begin{aligned}
\mathbf{D}_\mathbf{u} \mathbf{v} &= \{(\nabla \mathbf{v}) \mathbf{F}^{-1}(\mathbf{u})\}_s, \quad \mathbf{E}(\mathbf{u}_1, \mathbf{u}_2) = \frac{1}{2} \left\{ \mathbf{F}(\mathbf{u}_1)^T \mathbf{F}(\mathbf{u}_2) - \mathbf{I} \right\}_s, \\
\mathbf{S}(\mathbf{u}_1, \mathbf{u}_2) &= \lambda_s \text{tr}(\mathbf{E}(\mathbf{u}_1, \mathbf{u}_2)) \mathbf{I} + 2\mu_s \mathbf{E}(\mathbf{u}_1, \mathbf{u}_2).
\end{aligned}$$

Note that $\mathbf{S}(\mathbf{u}_1, \mathbf{u}_2) = \mathbf{S}^T(\mathbf{u}_1, \mathbf{u}_2) = \mathbf{S}(\mathbf{u}_2, \mathbf{u}_1)$.

Let $J^k := \det(\mathbf{F}(\mathbf{u}^k))$. For given finite element functions f^i , $i = 0, \dots, k$, \tilde{f}^k denote extrapolated values at $t = (k+1)\Delta t$, and $\left[\frac{\partial f}{\partial t} \right]^k$ stand for finite difference approximations of the time derivative at $t = k\Delta t$. For the case of the compressible Saint Venant–Kirchhoff material, the finite element method reads: Find $\{\mathbf{u}^{k+1}, \mathbf{v}^{k+1}, p^{k+1}\} \in \mathbb{V}_h^0 \times \mathbb{V}_h \times \mathbb{Q}_h$ such that $\mathbf{v}^{k+1} = \mathbf{g}_h(\cdot, (k+1)\Delta t)$ on Γ_{f0} , $\mathbf{v}^{k+1} = \mathbf{0}$ on Γ_{s0} and the following equations hold:

$$\begin{aligned}
 & \int_{\Omega_s} \rho_s \left[\frac{\partial \mathbf{v}}{\partial t} \right]^{k+1} \boldsymbol{\psi} \, \mathbf{d}\mathbf{x} + \int_{\Omega_s} \mathbf{F}(\tilde{\mathbf{u}}^k) \mathbf{S}(\mathbf{u}^{k+1}, \tilde{\mathbf{u}}^k) : \nabla \boldsymbol{\psi} \, \mathbf{d}\mathbf{x} \\
 & + \int_{\Omega_f} \rho_f \tilde{J}^k \left[\frac{\partial \mathbf{v}}{\partial t} \right]^{k+1} \boldsymbol{\psi} \, \mathbf{d}\mathbf{x} + \int_{\Omega_f} \rho_f \tilde{J}^k (\nabla \mathbf{v}^{k+1}) \mathbf{F}^{-1}(\tilde{\mathbf{u}}^k) \left(\mathbf{v}^k - \left[\frac{\partial \mathbf{u}}{\partial t} \right]^k \right) \boldsymbol{\psi} \, \mathbf{d}\mathbf{x} \\
 & + \int_{\Omega_f} 2\mu_f \tilde{J}^k \mathbf{D}_{\tilde{\mathbf{u}}^k} \mathbf{v}^{k+1} : \mathbf{D}_{\tilde{\mathbf{u}}^k} \boldsymbol{\psi} \, \mathbf{d}\mathbf{x} - \int_{\Omega_f} p^{k+1} \tilde{J}^k \mathbf{F}^{-T}(\tilde{\mathbf{u}}^k) : \nabla \boldsymbol{\psi} \, \mathbf{d}\mathbf{x} \\
 & + \int_{\Omega_f} \frac{\rho_f}{2} \left(\left[\frac{\partial J}{\partial t} \right]^k + \operatorname{div} \left(J^k \mathbf{F}^{-1}(\tilde{\mathbf{u}}^k) \left(\mathbf{v}^k - \left[\frac{\partial \mathbf{u}}{\partial t} \right]^k \right) \right) \right) \mathbf{v}^{k+1} \boldsymbol{\psi} \, \mathbf{d}\mathbf{x} = 0
 \end{aligned} \tag{17}$$

for all $\boldsymbol{\psi} \in \mathbb{V}_h^0$,

$$\int_{\Omega_s} \left[\frac{\partial \mathbf{u}}{\partial t} \right]^{k+1} \boldsymbol{\phi} \, \mathbf{d}\mathbf{x} - \int_{\Omega_s} \mathbf{v}^{k+1} \boldsymbol{\phi} \, \mathbf{d}\mathbf{x} = 0 \tag{18}$$

for all $\boldsymbol{\phi} \in \mathbb{V}_h^{00}$, and

$$\int_{\Omega_f} \tilde{J}^k (\nabla \mathbf{v}^{k+1}) : \mathbf{F}^{-T}(\tilde{\mathbf{u}}^k) q \, \mathbf{d}\mathbf{x} = 0 \tag{19}$$

for all $q \in \mathbb{Q}_h$. The integrals over the interface in (17) cancel out due to the interface condition (6). The coupling condition on Γ_{sf} is enforced strongly

$$\left[\frac{\partial \mathbf{u}}{\partial t} \right]^{k+1} = \mathbf{v}^{k+1} \quad \text{on } \Gamma_{sf}. \tag{20}$$

We note that the strong enforcement of the interface condition (20) together with (18) imply that the equality $\left[\frac{\partial \mathbf{u}}{\partial t} \right]^{k+1} = \mathbf{v}^{k+1}$ is satisfied in the usual sense in Ω_s . Eqs. (17)–(20) subject to initial conditions and a choice of continuous extension of \mathbf{u}^{k+1} from Ω_s onto Ω_f ensuring $\mathbf{u}^{k+1} \in \mathbb{V}_h^0$ define the discrete problem. In our numerical experiments, we shall use an extension based on an auxiliary elasticity equation, see Section 5.

Note that although strong coupling (20) is imposed on the interface, only a linear algebraic system should be solved on each time step. The finite element method (17)–(20) becomes the second order semi-implicit scheme if one sets

$$\tilde{f}^k := 2f^k - f^{k-1}, \quad \left[\frac{\partial f}{\partial t} \right]^k := \frac{3f^k - 4f^{k-1} + f^{k-2}}{2\Delta t}.$$

In the next section we study the energy stability of the first order finite element scheme (17)–(20).

Remark 1. The last term in (17) is consistent due to the identity (12) and is added in the FE formulation to enforce the conservation property of the discretization. While computations show that in practice this term can be skipped, numerical analysis in the next section benefits from including it. In the analysis of FEM for incompressible Navier–Stokes equations in the Eulerian description, including this term corresponds to the Temam’s [35] skew-symmetric form of the convective terms.

Remark 2. The following modifications to the finite element formulation should be made for the incompressible neo-Hookean material:

(i) Change the domain of integration in the pressure dependent term (sixths term in (17)) to the whole $\Omega(0)$, so it now reads:

$$- \int_{\Omega_s \cup \Omega_f} p^{k+1} \tilde{J}^k \mathbf{F}^{-T}(\tilde{\mathbf{u}}^k) : \nabla \boldsymbol{\psi} \, \mathbf{d}\mathbf{x}; \tag{21}$$

(ii) Replace the second term in (17) with

$$\mu_s \int_{\Omega_s} \mathbf{F}(\mathbf{u}^{k+1}) : \nabla \boldsymbol{\psi} \, \mathbf{d}\mathbf{x};$$

(iii) Consider the incompressibility condition in the form of identity (14) and add the following constraint to the finite element formulation:

$$\int_{\Omega_s} \tilde{J}^k \nabla \mathbf{v}^{k+1} : \mathbf{F}^{-T}(\tilde{\mathbf{u}}^k) q \, \mathbf{d}\mathbf{x} = 0 \quad \forall q \in \mathbb{Q}_h.$$

Hence instead of (19) we enforce the constraint in the whole reference domain $\Omega(0)$:

$$\int_{\Omega_s \cup \Omega_f} \tilde{J}^k (\nabla \mathbf{v}^{k+1}) : \mathbf{F}^{-T}(\tilde{\mathbf{u}}^k) q \, \mathbf{d}\mathbf{x} = 0 \quad \forall q \in \mathbb{Q}_h. \tag{22}$$

4. Stability analysis

In this section, we show energy balance and stability estimate for the solution to (17)–(20). We treat here only the first order method defined by setting

$$\tilde{f}^k = f^k, \quad \left[\frac{\partial \mathbf{v}}{\partial t} \right]^k := \frac{\mathbf{v}^k - \mathbf{v}^{k-1}}{\Delta t}, \quad \left[\frac{\partial \mathbf{u}}{\partial t} \right]^k := \frac{\mathbf{u}^k - \mathbf{u}^{k-2}}{2\Delta t}. \tag{23}$$

Moreover, for the clear analysis we make the third term in (17) “more explicit” replacing it with

$$\int_{\Omega_f} \rho_f J^{k-1} \left[\frac{\partial \mathbf{v}}{\partial t} \right]^{k+1} \boldsymbol{\psi} \, \mathbf{d}\mathbf{x}. \tag{24}$$

As common in the stability analysis, we consider the homogeneous boundary conditions on Γ_{f0} , i.e. $\mathbf{g} = \mathbf{0}$ in (7).

We first treat the case of the compressible Saint Venant–Kirchhoff material. Note the following identities:

$$\begin{aligned} 2 \left(\mathbf{E}(\mathbf{u}^k, \mathbf{u}^{k+1}) - \mathbf{E}(\mathbf{u}^{k-1}, \mathbf{u}^k) \right) &= \{ \mathbf{F}(\mathbf{u}^k)^T \mathbf{F}(\mathbf{u}^{k+1}) \}_s - \{ \mathbf{F}(\mathbf{u}^{k-1})^T \mathbf{F}(\mathbf{u}^k) \}_s \\ &= \{ \mathbf{F}(\mathbf{u}^k)^T \mathbf{F}(\mathbf{u}^{k+1}) \}_s - \{ \mathbf{F}(\mathbf{u}^k)^T \mathbf{F}(\mathbf{u}^{k-1}) \}_s \\ &= \{ \mathbf{F}(\mathbf{u}^k)^T (\mathbf{F}(\mathbf{u}^{k+1}) - \mathbf{F}(\mathbf{u}^{k-1})) \}_s \\ &= \{ \mathbf{F}(\mathbf{u}^k)^T (\nabla \mathbf{u}^{k+1} - \nabla \mathbf{u}^{k-1}) \}_s. \end{aligned} \tag{25}$$

Hence due to the symmetry of \mathbf{S} it holds

$$\begin{aligned} \mathbf{F}(\mathbf{u}^k) \mathbf{S}(\mathbf{u}^{k+1}, \mathbf{u}^k) : (\nabla \mathbf{u}^{k+1} - \nabla \mathbf{u}^{k-1}) &= \mathbf{S}(\mathbf{u}^{k+1}, \mathbf{u}^k) : \{ \mathbf{F}(\mathbf{u}^k)^T (\nabla \mathbf{u}^{k+1} - \nabla \mathbf{u}^{k-1}) \}_s \\ &= 2\mathbf{S}(\mathbf{u}^{k+1}, \mathbf{u}^k) : (\mathbf{E}(\mathbf{u}^k, \mathbf{u}^{k+1}) - \mathbf{E}(\mathbf{u}^{k-1}, \mathbf{u}^k)). \end{aligned} \tag{26}$$

Now we set in (17)

$$\boldsymbol{\psi} = \begin{cases} \left[\frac{\partial \mathbf{u}}{\partial t} \right]^{k+1} & \text{in } \Omega_s, \\ \mathbf{v}^{k+1} & \text{in } \Omega_f. \end{cases}$$

Thanks to (20), $\boldsymbol{\psi}$ is a suitable test function, i.e. $\boldsymbol{\psi} \in \mathbb{V}_h^0$. We handle each resulting term separately and start with the first term in (17):

$$\begin{aligned} \int_{\Omega_s} \rho_s \left[\frac{\partial \mathbf{v}}{\partial t} \right]^{k+1} \boldsymbol{\psi} \, \mathbf{d}\mathbf{x} &= \int_{\Omega_s} \rho_s \left(\frac{\mathbf{v}^{k+1} - \mathbf{v}^k}{\Delta t} \right) \left(\frac{\mathbf{u}^{k+1} - \mathbf{u}^{k-1}}{2\Delta t} \right) \, \mathbf{d}\mathbf{x} \\ &= \int_{\Omega_s} \rho_s \left(\frac{\mathbf{u}^{k+1} - \mathbf{u}^k - \mathbf{u}^{k-1} + \mathbf{u}^{k-2}}{(\Delta t)^2} \right) \left(\frac{\mathbf{u}^{k+1} - \mathbf{u}^{k-1}}{2\Delta t} \right) \, \mathbf{d}\mathbf{x} \end{aligned}$$

$$\begin{aligned}
 &= \frac{1}{2\Delta t} \int_{\Omega_s} \rho_s \left(\left| \frac{\mathbf{u}^{k+1} - \mathbf{u}^{k-1}}{2\Delta t} \right|^2 - \left| \frac{\mathbf{u}^k - \mathbf{u}^{k-2}}{2\Delta t} \right|^2 \right) \mathbf{d}\mathbf{x} \\
 &\quad + \frac{\Delta t}{2} \int_{\Omega_s} \rho_s \left| \frac{\mathbf{u}^{k+1} - \mathbf{u}^k - \mathbf{u}^{k-1} + \mathbf{u}^{k-2}}{2(\Delta t)^2} \right|^2 \mathbf{d}\mathbf{x}.
 \end{aligned} \tag{27}$$

Thanks to (25) and (26) we obtain for the second term in (17):

$$\begin{aligned}
 \int_{\Omega_s} \mathbf{F}(\mathbf{u}^k) \mathbf{S}(\mathbf{u}^{k+1}, \mathbf{u}^k) : \nabla \boldsymbol{\psi} \mathbf{d}\mathbf{x} &= \frac{1}{\Delta t} \int_{\Omega_s} \mathbf{S}(\mathbf{u}^{k+1}, \mathbf{u}^k) : (\mathbf{E}(\mathbf{u}^k, \mathbf{u}^{k+1}) - \mathbf{E}(\mathbf{u}^{k-1}, \mathbf{u}^k)) \mathbf{d}\mathbf{x} \\
 &= \frac{\lambda_s}{2\Delta t} \int_{\Omega_s} \left(\left[\text{tr}(\mathbf{E}(\mathbf{u}^k, \mathbf{u}^{k+1})) \right]^2 - \left[\text{tr}(\mathbf{E}(\mathbf{u}^{k-1}, \mathbf{u}^k)) \right]^2 \right) \mathbf{d}\mathbf{x} \\
 &\quad + \frac{\mu_s}{\Delta t} \int_{\Omega_s} (|\mathbf{E}(\mathbf{u}^k, \mathbf{u}^{k+1})|_F^2 - |\mathbf{E}(\mathbf{u}^{k-1}, \mathbf{u}^k)|_F^2) \mathbf{d}\mathbf{x} \\
 &\quad + \frac{\lambda_s}{2\Delta t} \int_{\Omega_s} \left[\text{tr}(\mathbf{E}(\mathbf{u}^k, \mathbf{u}^{k+1})) - \text{tr}(\mathbf{E}(\mathbf{u}^{k-1}, \mathbf{u}^k)) \right]^2 \mathbf{d}\mathbf{x} \\
 &\quad + \frac{\mu_s}{\Delta t} \int_{\Omega_s} \left| \mathbf{E}(\mathbf{u}^k, \mathbf{u}^{k+1}) - \mathbf{E}(\mathbf{u}^{k-1}, \mathbf{u}^k) \right|_F^2 \mathbf{d}\mathbf{x}.
 \end{aligned} \tag{28}$$

Straightforward computations show for the third term in (17):

$$\begin{aligned}
 \int_{\Omega_f} \rho_f J^{k-1} \left[\frac{\partial \mathbf{v}}{\partial t} \right]^{k+1} \boldsymbol{\psi} \mathbf{d}\mathbf{x} &= \int_{\Omega_f} \frac{\rho_f}{2} \frac{J^k |\mathbf{v}^{k+1}|^2 - J^{k-1} |\mathbf{v}^k|^2}{\Delta t} \mathbf{d}\mathbf{x} \\
 &\quad - \int_{\Omega_f} \frac{\rho_f |\mathbf{v}^{k+1}|^2}{2} \left[\frac{\partial J}{\partial t} \right]^k \mathbf{d}\mathbf{x} + \int_{\Omega_f} \frac{\Delta t \rho_f J^{k-1}}{2} \left| \left[\frac{\partial \mathbf{v}}{\partial t} \right]^{k+1} \right|^2 \mathbf{d}\mathbf{x}.
 \end{aligned} \tag{29}$$

Applying (15) to the fourth (inertia) term in (17) and using boundary and interface conditions give

$$\begin{aligned}
 \int_{\Omega_f} \rho_f J^k (\nabla \mathbf{v}^{k+1}) \mathbf{F}^{-1}(\mathbf{u}^k) \left(\mathbf{v}^k - \left[\frac{\partial \mathbf{u}}{\partial t} \right]^k \right) \boldsymbol{\psi} \mathbf{d}\mathbf{x} &= - \int_{\Omega_f} \frac{\rho_f}{2} \text{div} \left(J^k \mathbf{F}^{-1}(\mathbf{u}^k) \left(\mathbf{v}^k - \left[\frac{\partial \mathbf{u}}{\partial t} \right]^k \right) \right) |\mathbf{v}^{k+1}|^2 \mathbf{d}\mathbf{x} \\
 &\quad + \int_{\Gamma_{\text{out}}} \frac{\rho_f}{2} \mathbf{v}^k \cdot \mathbf{n} |\mathbf{v}^{k+1}|^2 \mathbf{d}\mathbf{s}.
 \end{aligned} \tag{30}$$

The fifth term in (17) gives

$$\int_{\Omega_f} \mu_f J^k \mathbf{D}_{\mathbf{u}^k}(\mathbf{v}^{k+1}) : \mathbf{D}_{\mathbf{u}^k} \boldsymbol{\psi} \mathbf{d}\mathbf{x} = \int_{\Omega_f} \mu_f J^k \left| \mathbf{D}_{\mathbf{u}^k}(\mathbf{v}^{k+1}) \right|_F^2 \mathbf{d}\mathbf{x},$$

and the next pressure term vanishes due to the incompressibility condition (19). Finally, the last term cancels with similar terms, but opposite signed, in (29) and (30). Substituting all equalities back into (17), we obtain after some cancellations the following energy balance for finite element FSI problem with the first order discretization in time:

$$\left. \begin{aligned}
 &\frac{1}{2} \int_{\Omega_s} \frac{\rho_s}{\Delta t} \left(\left| \left[\frac{\partial \mathbf{u}}{\partial t} \right]^{k+1} \right|^2 - \left| \left[\frac{\partial \mathbf{u}}{\partial t} \right]^k \right|^2 \right) \mathbf{d}\mathbf{x} \\
 &+ \frac{\rho_f}{2} \int_{\Omega_f} \frac{1}{\Delta t} \left(J^k |\mathbf{v}^{k+1}|^2 - J^{k-1} |\mathbf{v}^k|^2 \right) \mathbf{d}\mathbf{x}
 \end{aligned} \right\} \text{variation of kinetic energy}$$

$$\left. \begin{aligned}
 &+ \frac{\lambda_s}{2\Delta t} \left(\|\text{tr}(\mathbf{E}(\mathbf{u}^k, \mathbf{u}^{k+1}))\|_{\Omega_s}^2 - \|\text{tr}(\mathbf{E}(\mathbf{u}^{k-1}, \mathbf{u}^k))\|_{\Omega_s}^2 \right) \\
 &+ \frac{\mu_s}{\Delta t} \left(\|\mathbf{E}(\mathbf{u}^k, \mathbf{u}^{k+1})\|_{\Omega_s}^2 - \|\mathbf{E}(\mathbf{u}^{k-1}, \mathbf{u}^k)\|_{\Omega_s}^2 \right)
 \end{aligned} \right\} \text{variation of potential energy}$$

$$\begin{aligned}
 & + 2\mu_f \int_{\Omega_f} J^k \left| \mathbf{D}_{\mathbf{u}^k}(\mathbf{v}^{k+1}) \right|_F^2 \, \mathbf{d}\mathbf{x} \left. \vphantom{\int_{\Omega_f}} \right\} \begin{array}{l} \text{energy dissipation} \\ \text{in fluid} \end{array} \\
 & + \frac{\lambda_s \Delta t}{2} \left\| \frac{1}{\Delta t} (\text{tr}(\mathbf{E}(\mathbf{u}^k, \mathbf{u}^{k+1})) - \text{tr}(\mathbf{E}(\mathbf{u}^{k-1}, \mathbf{u}^k))) \right\|_{\Omega_s}^2 \\
 & + \mu_s \Delta t \left\| \frac{1}{\Delta t} (\mathbf{E}(\mathbf{u}^k, \mathbf{u}^{k+1}) - \mathbf{E}(\mathbf{u}^{k-1}, \mathbf{u}^k)) \right\|_{\Omega_s}^2 \\
 & + \frac{\rho_f(\Delta t)}{2} \int_{\Omega_f} J^{k-1} \left| \left[\frac{\partial \mathbf{v}}{\partial t} \right]^{k+1} \right|^2 \, \mathbf{d}\mathbf{x} \\
 & + \frac{\Delta t}{2} \left\| \rho_s^{\frac{1}{2}} \frac{\mathbf{u}^{k+1} - \mathbf{u}^k - \mathbf{u}^{k-1} + \mathbf{u}^{k-2}}{2(\Delta t)^2} \right\|_{\Omega_s}^2 \\
 & = -\frac{\rho_f}{2} \int_{\Gamma_{\text{out}}} \mathbf{v}^k \cdot \mathbf{n} |\mathbf{v}^{k+1}|^2 \, \mathbf{d}\mathbf{s} \left. \vphantom{\int_{\Gamma_{\text{out}}}} \right\} \begin{array}{l} \text{energy flux through} \\ \text{open boundary} \end{array}
 \end{aligned}
 \left. \vphantom{\int_{\Omega_s}} \right\} O(\Delta t) \text{ dissipative terms}$$

Here and further $\| \cdot \|_{\Omega_s}$ denotes the $L^2(\Omega_s)$ norm. One notes that the above equality resembles the energy balance (16) of the original FSI problem up to several $O(\Delta t)$ terms. In the structure these extra terms are always dissipative, while for the fluid we need the following assumption on the ALE displacement field. Assume that the extension of displacements to the fluid domain is such that for all k it holds $J^k > 0$ in Ω_f , i.e. the displacements do not tangle the mesh. For the sake of notation we shall also use $\| \cdot \|_{\Omega_f^k} := \left(\int_{\Omega_f} J^k | \cdot |^2 \, \mathbf{d}\mathbf{x} \right)^{\frac{1}{2}}$, which defines a k -dependent norm for $J^k > 0$. The terms in the fourth group on the left-hand side are non-negative and dropping them changes the equality to inequality. If Γ_{out} is always an outflow boundary or $\Gamma_{\text{out}} = \emptyset$, then the boundary term is non-negative and standing with minus sign it can be also dropped. We end up with the inequality:

$$\begin{aligned}
 & \frac{1}{2} \left\| \rho_s^{\frac{1}{2}} \left[\frac{\partial \mathbf{u}}{\partial t} \right]^{k+1} \right\|_{\Omega_s}^2 + \frac{\rho_f}{2} \|\mathbf{v}^{k+1}\|_{\Omega_f^k}^2 \\
 & + \frac{\lambda_s}{2} \|\text{tr}(\mathbf{E}(\mathbf{u}^k, \mathbf{u}^{k+1}))\|_{\Omega_s}^2 + \mu_s \|\mathbf{E}(\mathbf{u}^k, \mathbf{u}^{k+1})\|_{\Omega_s}^2 + 2\mu_f(\Delta t) \|\mathbf{D}_{\mathbf{u}^k}(\mathbf{v}^{k+1})\|_{\Omega_f^k}^2 \\
 & \leq \frac{1}{2} \left\| \rho_s^{\frac{1}{2}} \left[\frac{\partial \mathbf{u}}{\partial t} \right]^k \right\|_{\Omega_s}^2 + \frac{\rho_f}{2} \|\mathbf{v}^k\|_{\Omega_f^{k-1}}^2 + \frac{\lambda_s}{2} \|\text{tr}(\mathbf{E}(\mathbf{u}^{k-1}, \mathbf{u}^k))\|_{\Omega_s}^2 + \mu_s \|\mathbf{E}(\mathbf{u}^{k-1}, \mathbf{u}^k)\|_{\Omega_s}^2.
 \end{aligned}$$

To define the time-stepping method for $k = 0, 1$, we set $\mathbf{u}^{-2} := \mathbf{u}^{-1} := \mathbf{u}^0$. The energy estimate follows if we sum up the above inequalities for $k = 0, \dots, N - 1$:

$$\begin{aligned}
 & \frac{1}{2} \left\| \rho_s^{\frac{1}{2}} \left[\frac{\partial \mathbf{u}}{\partial t} \right]^N \right\|_{\Omega_s}^2 + \frac{\lambda_s}{2} \|\text{tr}(\mathbf{E}(\mathbf{u}^{N-1}, \mathbf{u}^N))\|_{\Omega_s}^2 + \mu_s \|\mathbf{E}(\mathbf{u}^{N-1}, \mathbf{u}^N)\|_{\Omega_s}^2 \\
 & + \frac{\rho_f}{2} \|\mathbf{v}_N\|_{\Omega_f^{N-1}}^2 + 2\mu_f \sum_{k=0}^{N-1} \Delta t \|\mathbf{D}_{\mathbf{u}^k}(\mathbf{v}^{k+1})\|_{\Omega_f^k}^2 \\
 & \leq \frac{\rho_f}{2} \|\mathbf{v}_0\|_{\Omega_f^0}^2 + \frac{\lambda_s}{2} \|\text{tr}(\mathbf{E}(\mathbf{u}^0, \mathbf{u}^0))\|_{\Omega_s}^2 + \mu_s \|\mathbf{E}(\mathbf{u}^0, \mathbf{u}^0)\|_{\Omega_s}^2.
 \end{aligned} \tag{31}$$

The analysis for the incompressible neo-Hookean material model follows the same lines. The second stress tensor term in (17) is different. It now gives:

$$\begin{aligned}
 & \frac{\mu_s}{2\Delta t} \int_{\Omega_s} \mathbf{F}(\mathbf{u}^{k+1}) : \nabla(\mathbf{u}^{k+1} - \mathbf{u}^{k-1}) \, \mathbf{d}\mathbf{x} = \frac{\mu_s}{2\Delta t} \int_{\Omega_s} \mathbf{F}(\mathbf{u}^{k+1}) : (\mathbf{F}(\mathbf{u}^{k+1}) - \mathbf{F}(\mathbf{u}^{k-1})) \, \mathbf{d}\mathbf{x} \\
 & = \frac{\mu_s}{4\Delta t} \int_{\Omega_s} |\mathbf{F}(\mathbf{u}^{k+1}) - \mathbf{F}(\mathbf{u}^{k-1})|_F^2 \, \mathbf{d}\mathbf{x} + \frac{\mu_s}{4\Delta t} \int_{\Omega_s} \left(|\mathbf{F}(\mathbf{u}^{k+1})|_F^2 - |\mathbf{F}(\mathbf{u}^{k-1})|_F^2 \right) \, \mathbf{d}\mathbf{x}.
 \end{aligned} \tag{32}$$

Table 1
Fluid and material parameters for FSI3 test.

ρ_s	λ_s	μ_s	ρ_f	μ_f
1000 kg/m ³	8000 000 Pa	2000 000 Pa	1000 kg/m ³	1 Pa s

Similar to (31), the summation over $k = 0, \dots, N - 1$ gives the a priori estimate:

$$\begin{aligned} & \frac{1}{2} \left\| \rho_s^{\frac{1}{2}} \left[\frac{\partial \mathbf{u}}{\partial t} \right]^N \right\|_{\Omega_s}^2 + \frac{\mu_s}{4} \|\mathbf{F}(\mathbf{u}^N)\|_{\Omega_s}^2 + \frac{\rho_f}{2} \|\mathbf{v}_N\|_{\Omega_f^{N-1}}^2 + 2\mu_f \sum_{k=0}^{N-1} \Delta t \|\mathbf{D}_{\mathbf{u}^k}(\mathbf{v}^{k+1})\|_{\Omega_f^k}^2 \\ & \leq \frac{\rho_f}{2} \|\mathbf{v}_0\|_{\Omega_f^0}^2 + \frac{\mu_s}{2} \|\mathbf{F}(\mathbf{u}^0)\|_{\Omega_s}^2. \end{aligned} \tag{33}$$

We summarize the results in the following theorem.

Theorem 1. Assume that the extension of the finite element displacement field to Ω_f is such that $\mathbf{J}^k > 0$ for all $k = 1, \dots, N - 1$, and Γ_{out} is always the outflow boundary or $\Gamma_{\text{out}} = \emptyset$. Then the solution to the finite element method (17)–(20), with extrapolation and time derivatives defined in (23), (24) satisfies the a priori estimate (31). For the incompressible material, the changes explained in Remark 2 are applied. In this case, the numerical solution satisfies the a priori estimate (33).

5. Numerical experiments

This section presents the numerical solution of two model FSI problems. The first problem is suggested in [36] for the purpose of benchmarking and is commonly used for the assessment of FSI numerical methods. For the second test, we simulate a 2D blood flow in a compliant vessel with aneurysm and compute flow statistics of interest. The second order in time variant of the semi-implicit finite element FSI scheme from Section 3 is used in all experiments. For the continuous extension of the displacement field in (1), we use the linear elasticity equation [37]

$$-\text{div}(\lambda_m(\text{div } \mathbf{u})\mathbf{I} + \mu_m(\nabla \mathbf{u} + \nabla \mathbf{u}^T)) = 0 \quad \text{in } \Omega_f, \tag{34}$$

with space dependent auxiliary parameters λ_m, μ_m .

We use P2-P1 (Taylor–Hood) elements for fluid variables and P2 elements for displacements. For the case of incompressible material, we experiment with globally continuous P1 elements for the Lagrange multiplier space \mathbb{Q}_h as well as with its extension admitting discontinuity across Γ_{fs} . An exact sparse factorization solver was applied to handle the linear algebraic system on each time step. We leave for the future research the development of preconditioned iterative methods based on ILU factorizations [38] for the resulting algebraic systems.

5.1. Flexible beam in 2D

We start with the unsteady flexible beam fluid–structure problem suggested in [36] as FSI3 test case. The problem was considered for the purpose of benchmarking by a number of authors, see [39] for the collection of results. An absolutely rigid circle of radius $r = 0.05$ and center $(0.2, 0.2)$ is placed in the two-dimensional rectangular domain $[0, 2.5] \times [0, 0.41]$. Here and further in Section 5.1 we use meters and seconds for distance and time units. A rectangular structure (a beam) of width 0.02 and length 0.35 with a mid-line passing through the center of the circle parallel to x -axis is attached to the circle. The fluid part Ω_f comprises the whole domain except the circle and the beam. The solid part Ω_s represents the beam only. The statistics of interest are the x - and y -deflection of the point $A(t)$ of the beam, with initial coordinates $A(0) = (0.6, 0.19)$, the drag and lift forces F_D, F_L exerted by the fluid on the whole body, i.e. the cylinder and the beam, and the frequencies f_1 and f_2 of x - and y -deflections of the beam, when a periodic motion is settled.

The beam is treated as a compressible Saint-Venant Kirchhoff structure. The fluid and material parameters are summarized in Table 1. On the inflow boundary the parabolic profile

$$v_1(0, y, t) = \frac{12}{0.1681} v(t)y(0.41 - y), \quad y \in [0, 0.41],$$

Table 2
Meshes for FSI3 test.

	# of cells in Ω_f	# of cells in Ω_s	# of active DOFs
Mesh 1	8 652	162	76 557
Mesh 2	17 540	334	154 242
Mesh 3	35 545	658	310 997

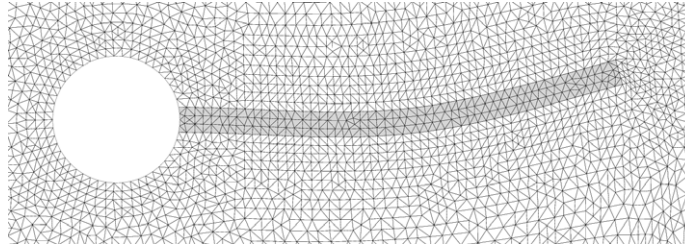


Fig. 1. Deformed (virtual) mesh at $t = 7.96$, corresponding to the largest displacement in a cross-flow direction. A part of the domain close to the cylinder and the beam is shown.

is prescribed, with

$$v(t) = \begin{cases} \frac{1}{2} \left(1 - \cos\left(\frac{\pi t}{2}\right) \right) & \text{for } t < 2, \\ 1 & \text{for } t \geq 2. \end{cases}$$

The outflow boundary is located at $x = 2.5$.

To apply the finite element method (17)–(20), we build three conforming meshes in the reference domain $\Omega_f \cup \Omega_s$, all of them are fitted to the fluid–structure interface and are locally refined in Ω_s and in the vicinity of the beam. The numbers of elements for all three meshes and corresponding numbers of degrees of freedom are given in Table 2. A zoom of mesh 2 is shown in Fig. 1.

The elasticity parameters in the extension equation (19) were taken *ad hoc* piecewise constant in Ω_f :

$$\lambda_m(\mathbf{x}) = \begin{cases} 20\lambda_s & \text{if the cell is adjacent to the beam,} \\ \lambda_s & \text{otherwise,} \end{cases}$$

$$\mu_m(\mathbf{x}) = \begin{cases} 20\mu_s & \text{if the cell is adjacent to the beam,} \\ \mu_s & \text{otherwise.} \end{cases}$$

The increased stiffness for small mesh elements near the beam provides more uniform mesh deformation over the fluid domain, thus ensuring $J \geq c_0 > 0$ in Ω_f , see [40].

The simulations were run with fixed time steps until the final time $t = 8$. By the time $t = 4$, the computed solution attains an unsteady periodic regime. The velocity field of the periodic solution computed with Mesh 2 at $t = 8$ is shown in Fig. 2. The street of vortices detaching from the structure is clearly seen. Fig. 3 shows the graphs of displacements $u_1(A(t))$ and $u_2(A(t))$ on time interval [7, 8].

The flow and structure statistics of interest computed for the three meshes and with time steps $\Delta t \in \{4 \cdot 10^{-3}, 2 \cdot 10^{-3}, 10^{-3}\}$ are summarized in Table 3. They were computed for the time interval [7, 8]. The mean values of the displacements and forces were calculated by averaging the maximum and the minimum values over the time interval [7, 8]. The periods f_1 and f_2 are computed by measuring time lapses between peak values. All statistics converge when the spatial mesh and time step are refined (the best resolution is shown in the bold font). The converged values are in good agreement with the results from [39] computed with other approaches, using at least 50,000 degrees of freedom, and with results from [41] computed with higher order finite elements and as many as 525,226 degrees of freedom.

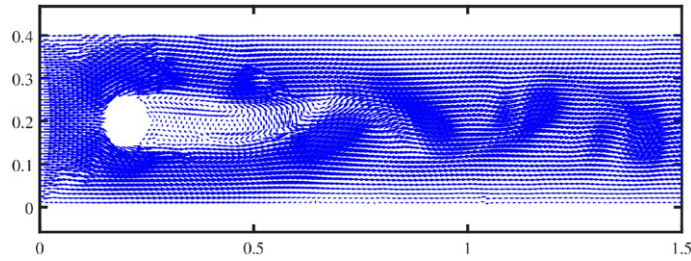


Fig. 2. The velocity vector field of the periodic solution at $t = 8$.

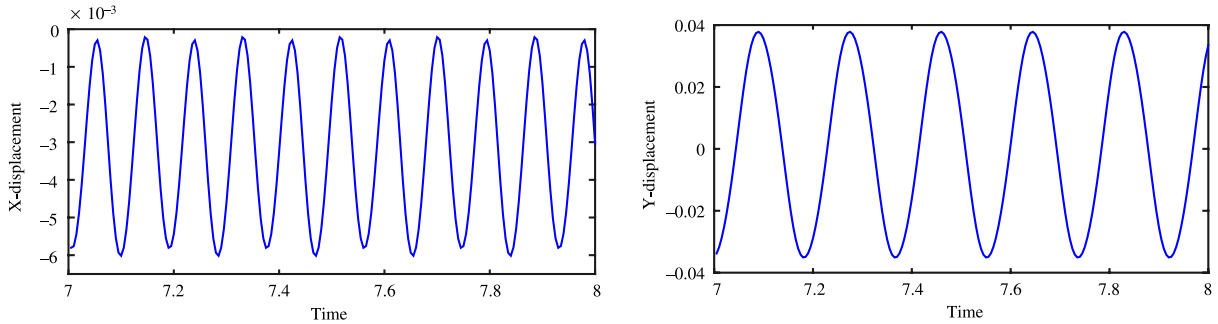


Fig. 3. The plots of the x - and y -deflections of the beam at point A.

Table 3

Computed statistics for FSI3 test for the time interval [7, 8], reference intervals based on various results from [39], and reference values from [41].

Mesh	Time step	$u_1(A) \cdot 10^3$	$u_2(A) \cdot 10^3$	F_D	F_L	f_1	f_2
1	10^{-3}	-2.8 ± 2.6	1.5 ± 34.3	432.9 ± 22.3	0.98 ± 152.1	10.81	5.48
2	10^{-3}	-3.0 ± 2.8	1.4 ± 35.9	453.8 ± 26.8	2.6 ± 154.0	10.81	5.41
3	10^{-3}	-3.0 ± 2.9	1.4 ± 36.1	458.0 ± 27.6	3.0 ± 154.5	10.81	5.40
3	$2 \cdot 10^{-3}$	-3.0 ± 2.8	1.4 ± 35.9	458.4 ± 26.7	3.2 ± 152.3	10.87	5.43
3	$4 \cdot 10^{-3}$	-3.0 ± 2.8	1.4 ± 35.7	459.2 ± 26.1	3.8 ± 143.0	10.87	5.43
[39]		$[-3.04, -2.84]$ $\pm [2.67, 2.87]$	$[1.28, 1.55]$ $\pm [34.61, 46.63]$	$[452.4, 474.9]$ $\pm [26.19, 36.63]$	$[1.81, 3.86]$ $\pm [152.7, 165.9]$	$[10.84, 11.63]$	$[4.98, 5.46]$
[41]		-2.91 ± 2.74	1.46 ± 35.2	460.3 ± 27.67	2.41 ± 157	10.95	5.48

5.2. Blood flow in a vessel with aneurysm

Our second test case is a variant of the 2D hemodynamic model problem from [42]. The computational domain $\Omega(0) \subset [-8, 0] \times [0, 8]$ and the grid are shown in Fig. 4. In Section 5.2 we use millimeters and seconds for distance and time units. The shaded part is the structure (the compliant wall of the vessel) and the rest is the fluid domain. The dilatation of the vessel models an aneurysm. The aneurysm wall is typically thinner than that of the healthy artery part, which can lead to possible rupture and bleeding. The goal of this numerical experiment is to demonstrate the reliability of the semi-implicit finite element method (17)–(20) for the hemodynamic simulations. We shall also study the influence of elasticity model parameters on the flow dynamics and the wall response for aneurysm.

In [42], the authors look at the difference of flow dynamics depending on whether the vessels wall is treated as rigid or neo-Hookean compressible material. Here we are interested in the response of the system towards the variation of material parameters and constitutive relations describing the elastic structure. In particular, we compare compressible and incompressible elasticity models for the walls. For the compressible case, we use the neo-Hookean material with Cauchy stress tensor given by

$$\sigma_s = \frac{\mu_s}{J^2} \left(\mathbf{F}\mathbf{F}^T - \frac{1}{2} \text{tr}(\mathbf{F}\mathbf{F}^T) \mathbf{I} \right) + \left(\lambda_s + \frac{2\mu_s}{3} \right) (J - 1) \mathbf{I}. \tag{35}$$

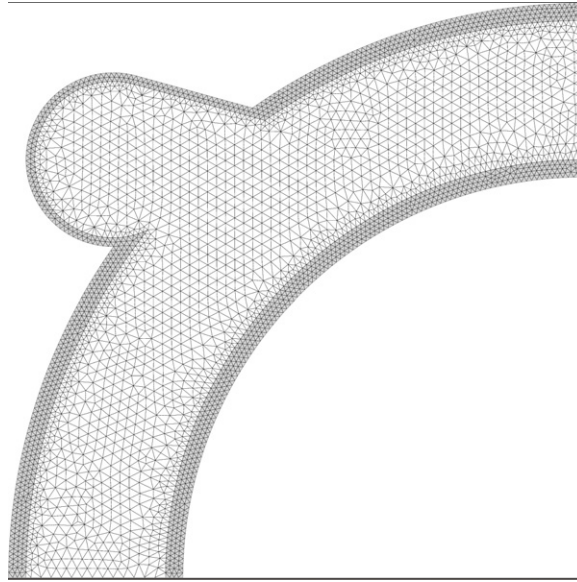


Fig. 4. The triangulated computational domain for the model hemodynamic problem. The upper open part of the boundary is the inflow. The bottom open part of the boundary serves as the outflow.

The constitutive relation is different from the St. Venant–Kirchhoff model in (10) and is not covered by the analysis of the paper. Numerical experiments, however, show stability of the semi-implicit finite element method in this case as well.

Since we are interested in having a linear system of equations on every time step, we perform the time discretization of the elasticity part in the case of the neo-Hookean law as follows. The first Piola–Kirchhoff stress tensor is

$$\mathbf{P} = \frac{\mu_s}{J} \left(\mathbf{F} - \frac{1}{2} \text{tr}(\mathbf{F}\mathbf{F}^T) \mathbf{F}^{-T} \right) + \left(\lambda_s + \frac{2\mu_s}{3} \right) J(J-1) \mathbf{F}^{-T}.$$

In 2D, taking into account

$$\mathbf{F}^{-T} = \frac{1}{J} (\mathbf{I} + \hat{\nabla} \mathbf{u}), \quad \text{tr}(\mathbf{F}\mathbf{F}^T) = 2 + 2 \text{div } \mathbf{u} + \nabla \mathbf{u} : \nabla \mathbf{u}, \quad J = 1 + \text{div } \mathbf{u} + \frac{1}{2} \hat{\nabla} \mathbf{u} : \nabla \mathbf{u},$$

the first Piola–Kirchhoff stress tensor can be rewritten as

$$\mathbf{P} = \frac{\mu_s}{J} \nabla \mathbf{u} + \frac{\mu_s}{2J^2} (\hat{\nabla} \mathbf{u} : \nabla \mathbf{u} - \nabla \mathbf{u} : \nabla \mathbf{u}) \mathbf{I} - \frac{\mu_s}{J^2} \left(1 + \text{div } \mathbf{u} + \frac{1}{2} \nabla \mathbf{u} : \nabla \mathbf{u} \right) \hat{\nabla} \mathbf{u} + \left(\lambda_s + \frac{2\mu_s}{3} \right) J(J-1) \mathbf{F}^{-T}$$

with $\hat{\nabla} \mathbf{u} = \begin{pmatrix} \frac{\partial u_2}{\partial y} & -\frac{\partial u_2}{\partial x} \\ -\frac{\partial u_1}{\partial y} & \frac{\partial u_1}{\partial x} \end{pmatrix}$. We use the following linearization at time step $k + 1$:

$$\begin{aligned} \mathbf{P}^{k+1} \approx & \frac{\mu_s}{\tilde{J}^k} \nabla \mathbf{u}^{k+1} + \frac{\mu_s}{2(\tilde{J}^k)^2} ((\hat{\nabla} \tilde{\mathbf{u}}^k - \nabla \tilde{\mathbf{u}}^k) : \nabla \mathbf{u}^{k+1}) \mathbf{I} - \frac{\mu_s}{(\tilde{J}^k)^2} \left(1 + \text{div } \tilde{\mathbf{u}}^k + \frac{1}{2} \nabla \tilde{\mathbf{u}}^k : \nabla \tilde{\mathbf{u}}^k \right) \hat{\nabla} \mathbf{u}^{k+1} \\ & + \left(\lambda_s + \frac{2\mu_s}{3} \right) \left(\left(1 + \frac{\partial \tilde{u}_2}{\partial y} \right)^k \frac{\partial u_1}{\partial x}^{k+1} - \frac{\partial \tilde{u}_2}{\partial x}^k \frac{\partial u_1}{\partial y}^{k+1} + \frac{\partial u_2}{\partial y}^{k+1} \right) (\mathbf{I} + \hat{\nabla} \tilde{\mathbf{u}}^k). \end{aligned}$$

In the incompressible case, we use the elasticity model defined in (11). We take the same μ_s for both models, and vary λ_s in (35) to change the response to compressional deformations. In the limit $\lambda_s \rightarrow \infty$, the above neo-Hookean model is expected to behave similarly to the incompressible one with respect to compressional deformations. We shall see that this is the case in the discrete setting only if one allows finite element Lagrange multiplier to be discontinuous across Γ_{fs} .

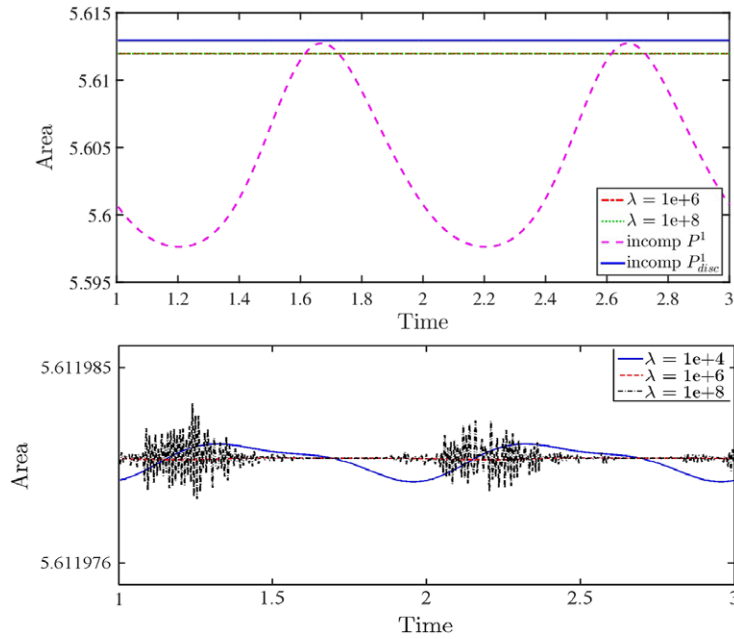


Fig. 5. Both plots show the evolution of the area of Ω_s for different models of vessel wall: neo-Hookean compressible and neo-Hookean incompressible. The bottom plot excludes the incompressible case and shows the area evolution for the other models in a different scale.

Table 4
Fluid and material parameters for the blood flow in a vessel test.

ρ_s	μ_s	ρ_f	μ_f
$1.12 \cdot 10^3 \text{ kg/m}^3$	270 000 Pa	$1.035 \cdot 10^3 \text{ kg/m}^3$	$3.4983 \cdot 10^{-3} \text{ Pa s}$

Following [42], we impose the pulsatile incoming flow according to

$$v_1(0, y, t) = -50(8 - y)(y - 6)(1 + 0.75 \sin(2\pi t)), \quad 6 \leq y \leq 8.$$

The upper and lower ends of the artery walls are fixed. The flow and material parameters are given in Table 4. The values of ρ_s , ρ_f , and μ_f are taken from [42], while the shear modulus μ_s is taken from [43], where it was experimentally measured for a dog’s artery. The time step is equal to 10^{-3} . Finally, for the extension equation (34), we set $\mu_m = \mu_s$ and $\lambda_m = 4\lambda_s$. For the compressible material, the second parameter was varied: $\lambda_s \in \{10^4, 10^6, 10^8\}$ kPa. The corresponding Poisson’s ratios $\nu = \frac{1}{2}\lambda_s/(\lambda_s + \mu_s)$ are equal to 0.4869, 0.499865 and 0.49999865, respectively.

First we compute the area of the solid domain over the time interval [1, 3] for different elasticity models. Fig. 5 shows how the area of the solid domain changes over time. In this figure and further in the text, P^1 marks results with globally continuous P^1 space \mathbb{Q}_h , while P^1_{disc} marks results with \mathbb{Q}_h discontinuous across Γ_{fs} . Two phenomena become apparent. First, for the large values of the second elasticity parameter λ_s , the neo-Hookean compressible model produces minor variations of the walls volume comparable to those shown by the incompressible model with discontinuous finite element Lagrange multiplier. Otherwise, using globally continuous P^1 elements for \mathbb{Q}_h space leads to a noticeable deviation of the structure area from the reference value. This phenomena is numerical and results from the inconsistency between the continuity of functions in \mathbb{Q}_h and the non-matching of the interface values of fluid pressure and the multiplier p_s in the structure. One may expect the numerical inconsistency to decay for a finer mesh. This is what experiments demonstrate. Indeed, Fig. 6 shows the variation of $\text{area}(\Omega_s)$ for the mesh shown in Fig. 4 and for a finer mesh with 3 and 6 layers of triangles in the aneurysm and the healthy part of the vessel wall, respectively. The mesh in the fluid domain was correspondingly modified to match the refined mesh in Ω_s . The results in Fig. 6 suggest the mesh-convergence of the finite element incompressible model to the ‘true’ incompressible

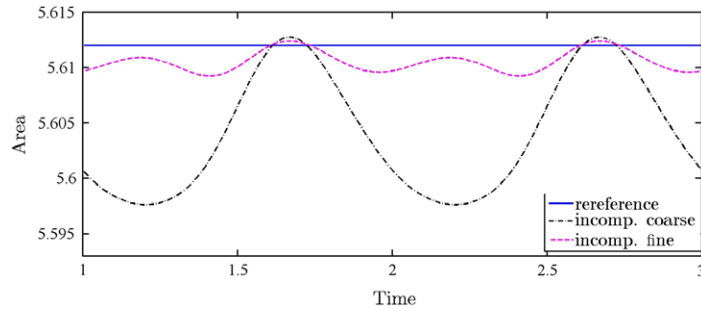


Fig. 6. The plot demonstrates the improvement in the area conservation by the finite element incompressible model if the mesh is refined.

limit (the ‘reference’ is the area in the incompressible limit). The second phenomena clearly seen in Fig. 5 is the development of non-physical oscillations for $\lambda_s = 10^8$ kPa. These oscillations are small in amplitude (note the scaling of the ‘area’ axis). They may result from solving algebraic systems with poor conditioned matrices in finite precision arithmetics. A closer look at this phenomena requires additional studies. Such studies will be done elsewhere. We remark that we also experimented with the enforcement of the incompressibility condition through the linearized $J - 1 = 0$ condition and using the same space for the finite element Lagrange multiplier. We observed results close to those computed with the enforcement of the incompressibility condition using (22), but we have no analysis of this modified finite element method.

Wall shear stress (WSS) values is another statistic of common interest. According to [44] measuring WSS peak values along the vessel wall is crucial in estimating the risk of both aneurysm formation in the initial stages and the eventual rupture. In Fig. 7, we present the maximum and the average of the absolute values of WSS evaluated along the dilatation wall. The overprediction of the WSS is seen for the incompressible case, if globally continuous finite element Lagrange multiplier is used.

6. Conclusion

In this paper we focused on the numerical model of FSI involving incompressible viscous Newtonian fluid and hyperelastic compressible or incompressible material. The monolithic finite element method based on Arbitrary Lagrangian–Eulerian formulation was addressed. Within this approach the fluid and solid equations are discretized in a triangulated reference domain. We introduced the semi-explicit time discretization, which leads to a linear system to be solved on every time step and the strong enforcement of coupling conditions on the fluid–structure interface. This yields the numerically stable FSI method which avoids inner iterations between subdomains. The energy balance and stability estimate for the numerical solutions were shown in the fully discrete setting and without any model simplifications or time-step restrictions. An assumption was that the ALE displacement field in the fluid domain should provide an untangled (virtual) triangulation. This may limit the method to simulations of problems where the structure displacements are moderate and no topological changes occur. The finite element method was numerically tested on the benchmark FSI3 problem from [39] and the model hemodynamic problem for the flow in the compliant vessel with aneurysm [42]. The numerical results confirmed the stability and numerical efficiency of the FSI algorithm.

Since our approach treats compressible and incompressible materials in a unified manner, we experimented with the dependence of flow statistics on the choice of the model and parameters of the model. We found that in the finite element setting, when the incompressibility constraint is enforced weakly using globally continuous Lagrange multiplier, the numerical inconsistency may lead to noticeable errors in structure volume and predicted wall shear stresses. Computed results for a compressible material with Poisson ratio approaching $\frac{1}{2}$ were found to be close to those for the purely incompressible case with the numerically consistent choice of discontinuous at interface Γ_{fs} Lagrange multipliers.

Acknowledgment

We are grateful to Annalisa Quaini for informative and fruitful discussions.

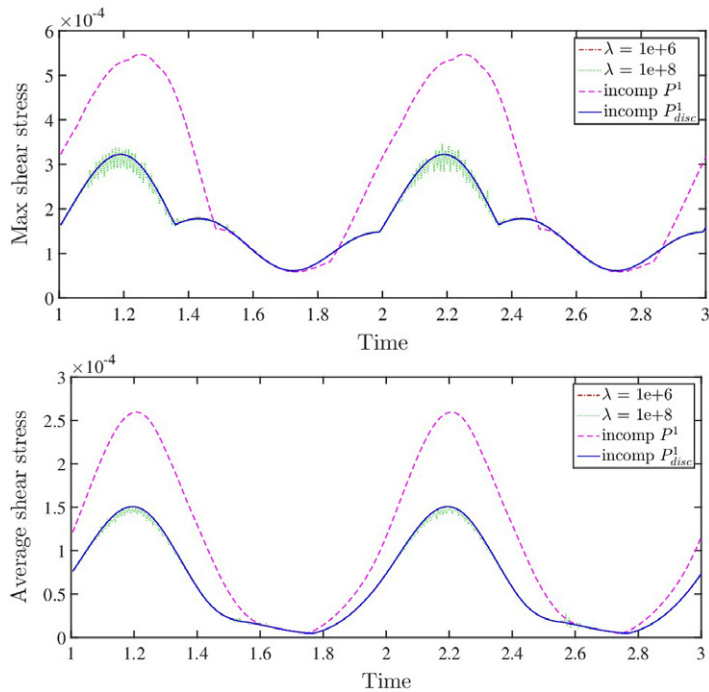


Fig. 7. The absolute value of the wall shear stress on the inside of the aneurysm wall; Top: maximum along the wall; Bottom: average along the wall.

References

- [1] T. Bodnár, G.P. Galdi, Š Nečasová, *Fluid–Structure Interaction and Biomedical Applications*, Springer, 2014.
- [2] L. Formaggia, A. Quarteroni, A. Veneziani, *Cardiovascular Mathematics: Modeling and Simulation of the Circulatory System*, vol. 1, Springer Science & Business Media, 2010.
- [3] J. Tu, K. Inthavong, K.K.L. Wong, *Computational Hemodynamics—Theory, Modelling and Applications*, Springer, 2015.
- [4] G. Hou, J. Wang, A. Layton, Numerical methods for fluid–structure interaction—a review, *Commun. Comput. Phys.* 12 (2) (2012) 337–377.
- [5] J. Hron, S. Turek, *A Monolithic FEM/multigrid Solver for an ALE Formulation of Fluid–structure Interaction with Applications in Biomechanics*, Springer, Berlin, Heidelberg, 2006.
- [6] B. Hubner, E. Walhorn, D. Dinkler, A monolithic approach to fluid–structure interaction using space–time finite elements, *Comput. Methods Appl. Mech. Engrg.* 193 (23) (2004) 2087–2104.
- [7] C. Michler, S.J. Hulshoff, E.H. van Brummelen, R. de Borst, A monolithic approach to fluid–structure interaction, *Comput. & Fluids* 33 (5) (2004) 839–848.
- [8] P.B. Ryzhakov, R. Rossi, S.R. Idelsohn, E. Onate, A monolithic Lagrangian approach for fluid–structure interaction problems, *Comput. Mech.* 46 (6) (2010) 883–899.
- [9] S. Badia, F. Nobile, C. Vergara, Fluid–structure partitioned procedures based on robin transmission conditions, *J. Comput. Phys.* 227 (14) (2008) 7027–7051.
- [10] J. Degroote, P. Bruggeman, R. Haelterman, J. Vierendeels, Stability of a coupling technique for partitioned solvers in FSI applications, *Comput. Struct.* 86 (23) (2008) 2224–2234.
- [11] J. Degroote, R. Haelterman, S. Annerel, P. Bruggeman, J. Vierendeels, Performance of partitioned procedures in fluid–structure interaction, *Comput. Struct.* 88 (7) (2010) 446–457.
- [12] D. Mok, W. Wall, Partitioned analysis schemes for the transient interaction of incompressible flows and nonlinear flexible structures, in: *Trends in Computational Structural Mechanics*, Barcelona.
- [13] P. Causin, J.F. Gerbeau, F. Nobile, Added-mass effect in the design of partitioned algorithms for fluid–structure problems, *Comput. Methods Appl. Mech. Engrg.* 194 (42) (2005) 4506–4527.
- [14] C. Förster, W.A. Wall, E. Ramm, Artificial added mass instabilities in sequential staggered coupling of nonlinear structures and incompressible viscous flows, *Comput. Methods Appl. Mech. Engrg.* 196 (7) (2007) 1278–1293.
- [15] M.A. Fernández, M. Moubachir, A newton method using exact Jacobians for solving fluid–structure coupling, *Comput. Struct.* 83 (2) (2005) 127–142.
- [16] P. Kuberry, H. Lee, A decoupling algorithm for fluid–structure interaction problems based on optimization, *Comput. Methods Appl. Mech. Engrg.* 267 (2013) 594–605.
- [17] F. Nobile, Numerical approximation of fluid–structure interaction problems with application to haemodynamics (Ph.D. thesis), Politecnico di Milano, 2001.

- [18] M.A. Fernández, J.-F. Gerbeau, C.A. Grandmont, A projection semi-implicit scheme for the coupling of an elastic structure with an incompressible fluid, *Internat. J. Numer. Methods Engrg.* 69 (4) (2007) 794–821.
- [19] S. Badia, A. Quaini, A. Quarteroni, Modular vs. non-modular preconditioners for fluid–structure systems with large added-mass effect, *Comput. Methods Appl. Mech. Engrg.* 197 (49) (2008) 4216–4232.
- [20] C. Grandmont, V. Guimet, Y. Maday, Numerical analysis of some decoupling techniques for the approximation of the unsteady fluid structure interaction, *Math. Models Methods Appl. Sci.* 11 (08) (2001) 1349–1377.
- [21] E. Swim, P. Seshaiyer, A nonconforming finite element method for fluid–structure interaction problems, *Comput. Methods Appl. Mech. Engrg.* 195 (17) (2006) 2088–2099.
- [22] J. Donea, S. Giuliani, J.P. Halleux, An arbitrary Lagrangian–Eulerian finite element method for transient dynamic fluid–structure interactions, *Comput. Methods Appl. Mech. Engrg.* 33 (1) (1982) 689–723.
- [23] C.W. Hirt, A.A. Amsden, J.L. Cook, An arbitrary Lagrangian–Eulerian computing method for all flow speeds, *J. Comput. Phys.* 14 (3) (1974) 227–253.
- [24] T.J.R. Hughes, W.K. Liu, T.K. Zimmermann, Lagrangian–Eulerian finite element formulation for incompressible viscous flows, *Comput. Methods Appl. Mech. Engrg.* 29 (3) (1981) 329–349.
- [25] S. Canic, B. Muha, M. Bukac, Fluid–structure interaction in hemodynamics: Modeling, analysis, and numerical simulation, in: T. Bodnar, G.P. Galdi, S. Necasova (Eds.), *Fluid–Structure Interaction and Biomedical Applications, Advances in Mathematical Fluid Mechanics*, Springer, Basel, 2014, pp. 79–195. http://dx.doi.org/10.1007/978-3-0348-0822-4_2.
- [26] P. Crosetto, P. Reymond, S. Deparis, D. Kontaxakis, N. Stergiopoulos, A. Quarteroni, Fluid–structure interaction simulation of aortic blood flow, *Comput. & Fluids* 43 (1) (2011) 46–57.
- [27] M.A. Fernández, J.-F. Gerbeau, Algorithms for fluid–structure interaction problems, in: *Cardiovascular Mathematics*, Springer, 2009, pp. 307–346.
- [28] I. Ozolanta, G. Tetera, B. Purinya, V. Kasyanov, Changes in the mechanical properties, biochemical contents and wall structure of the human coronary arteries with age and sex, *Med. Eng. Phys.* 20 (7) (1998) 523–533.
- [29] R.P. Vito, S.A. Dixon, Blood vessel constitutive models-1995-2002, *Ann. Rev. Biomed. Eng.* 5 (1) (2003) 413–439.
- [30] Z. Yosibash, I. Manor, I. Gilad, U. Willentz, Experimental evidence of the compressibility of arteries, *J. Mech. Behav. Biomed. Mater.* 39 (2014) 339–354.
- [31] Z. Yosibash, E. Priel, p-FEMs for hyperelastic anisotropic nearly incompressible materials under finite deformations with applications to arteries simulation, *Internat. J. Numer. Methods Engrg.* 88 (11) (2011) 1152–1174.
- [32] K. Lipnikov, Y. Vassilevski, A. Danilov, et al. *Advanced Numerical Instruments 2D*, <http://sourceforge.net/projects/ani2d>.
- [33] T.E. Tezduyar, S. Sathe, T. Cragin, B. Nanna, B. Conklin, J. Pausewang, M. Schwaab, Modelling of fluid–structure interactions with the space–time finite elements: Arterial fluid mechanics, *Internat. J. Numer. Methods Fluids* 54 (6–8) (2007) 901–922.
- [34] T.E. Tezduyar, S. Sathe, K. Stein, Solution techniques for the fully discretized equations in computation of fluid–structure interactions with the space–time formulations, *Comput. Methods Appl. Mech. Engrg.* 195 (41) (2006) 5743–5753.
- [35] R. Temam, *Navier–Stokes Equations: Theory and Numerical Analysis*, vol. 343, American Mathematical Soc., 2001.
- [36] S. Turek, J. Hron, Proposal for numerical benchmarking of fluid–structure interaction between an elastic object and laminar incompressible flow, in: H.-J. Bungartz, M. Schäfer (Eds.), *Fluid-Structure Interaction*, in: *Lecture Notes in Computational Science and Engineering*, vol. 53, Springer, Berlin, Heidelberg, 2006, pp. 371–385. http://dx.doi.org/10.1007/3-540-34596-5_15.
- [37] P.A. Sackinger, P.R. Schunk, R.R. Rao, A Newton–Raphson pseudo-solid domain mapping technique for free and moving boundary problems: a finite element implementation, *J. Comput. Phys.* 125 (1) (1996) 83–103.
- [38] I.N. Konshin, M.A. Olshanskii, Y.V. Vassilevski, ILU preconditioners for non-symmetric saddle point matrices with application to the incompressible Navier–Stokes equations, *SIAM J. Sci. Comput.* 37 (2015) A2171–A2197.
- [39] S. Turek, J. Hron, M. Razaq, H. Wobker, M. Schäfer, Numerical benchmarking of fluid–structure interaction: A comparison of different discretization and solution approaches, in: H.-J. Bungartz, M. Mehl, M. Schäfer (Eds.), *Fluid Structure Interaction II*, in: *Lecture Notes in Computational Science and Engineering*, vol. 73, Springer, Berlin, Heidelberg, 2010, pp. 413–424. http://dx.doi.org/10.1007/978-3-642-14206-2_15.
- [40] K. Stein, T.E. Tezduyar, R. Benney, Mesh moving techniques for fluid–structure interactions with large displacements, *J. Appl. Mech.* 70 (1) (2003) 58–63.
- [41] J. Liu, A second-order stable explicit interface advancing scheme for fsi with both rigid and elastic structures and its application to fish swimming simulations, *Comput. & Fluids* (2015) <http://dx.doi.org/10.1016/j.compfluid.2015.06.002>.
- [42] S. Turek, J. Hron, M. Madlik, M. Razaq, H. Wobker, J. Acker, Numerical simulation and benchmarking of a monolithic multigrid solver for fluid–structure interaction problems with application to hemodynamics, in: H.-J. Bungartz, M. Mehl, M. Schäfer (Eds.), *Fluid Structure Interaction II*, in: *Lecture Notes in Computational Science and Engineering*, vol. 73, Springer, Berlin, Heidelberg, 2010, pp. 193–220. http://dx.doi.org/10.1007/978-3-642-14206-2_8.
- [43] C.G. Karo, T.J. Pedley, R.C. Schroder, W.A. Seed, *The Mechanics of the Circulation*, Oxford University Press, 1978.
- [44] M. Shojima, M. Oshima, K. Takagi, R. Torii, M. Hayakawa, K. Katada, A. Morita, T. Kirino, Magnitude and role of wall shear stress on cerebral aneurysm computational fluid dynamic study of 20 middle cerebral artery aneurysms, *Stroke* 35 (11) (2004) 2500–2505.